HDice Technical Note 28

Development of fast rasters for eHD test runs and experiments

C. D. Bass

July 25, 2013

Abstract

The polarized HD targets used during the 2012 eHD irradiation tests showed signs of excessive heating from electron beam energy deposition in the target. The Hall B raster used for these tests was not fast enough to move the electron beam spot across the target, which resulted in substantial temperature spikes. An existing 6-GeV raster system previously used in Halls A and C could be used to substantially lower the magnitude of temperature spikes. Such a fast raster, combined with an improved HD target cell design, is expected to result in much lower operating temperatures in future eHD measurements. A new 11-GeV raster system would need to be developed for eHD experiments at higher energies. This report details the performance of the existing Hall B and 6-GeV raster systems and provides design specifications for an 11-GeV raster system.

1 Rastering experiences during the 2012 eHD tests

During the February 2012 and March 2012 eHD test runs, H- and D-polarization losses were measured using NMR. Subsequent calculations indicated that the target cell design and electron beam rastering system were inadequate and resulted in significant heating of target material from Møller scattering. The design of the g14 target was optimized for γHD runs and not for the removal of heat due to electron beam interaction with the target. A redesign of the target cell for improved heat removal is being developed for eHD experiments and will be discussed in a future technical note.

Local heating of target material due to electron beam energy deposition is a function of current density, irradiation time, specific heat capacities of target materials, and the base target temperature (see Appendix A). Current density is determined by the beam current and spot size at the target. The choice of beam current is a compromise between experimental data rates and target irradiation effects such as depolarization from radiation damage.

The beam spot size is constrained by beam line optics and the rate of high-energy electron interactions with high-Z material surrounding the target (e.g. copper). The arrangement of focusing and steering magnets on the beam line produces a beam with an approximately Gaussian density profile and sets a minimum beam radius of about 50 μm.

High-energy electrons that irradiate high-Z materials surrounding the target can generate a cascade shower of gamma-rays and electron-positron pairs. Limiting the shower production rate places a constraint on the allowable current density in the radial tail of the beam that extends beyond the edge of the target, and so determines a minimum separation distance between the centroid of the beam and the edge of the target. Increasing the beam spot size to lower the current density will reduce the target volume that is available for uniform irradiation and creates a zone

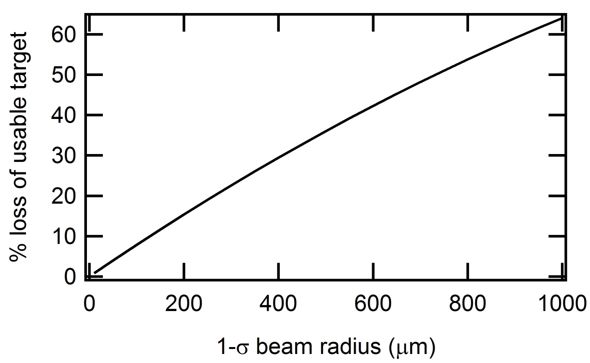

Figure 1: Plot of the percentage loss of usable target material as a function of intrinsic beam spot size for a 25 mm diameter target. The loss of useful target material is due to the requirement that the 5σ radius of the beam be within the target.

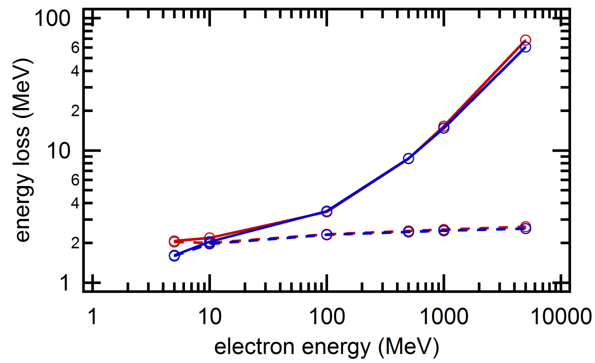

Figure 2: Plot of the calculated electron total energy loss (solid lines) and energy deposition (dashed lines) through 5 cm of target material comprised of HD and aluminum ($\sim$5:1 mass ratio). The calculations were performed using GEANT [1] (blue curves) and ESTAR [2] (red curves). Both programs encompass the same basic electron interaction mechanisms, but approximate subtle effects in different ways (e.g. atomic excitations, reduction in stopping power due to polarization of the medium by the charged beam).

in the outer layer of target material that experiences smaller beam-related polarization losses. For a 1 nA beam, the rate limit for high-energy electron interactions within the copper ring that surrounds the target occurs at the beam's 5-σ radius, and Figure 1 shows the loss of usable target material as a function of beam diameter. Practically, this limits the 1-σ radius of the beam spot on target to a few hundred microns.

Target irradiation time can be reduced by pulsing the beam or periodically moving the beam spot to different locations on the target that are (approximately) thermally isolated from each other. Pulsing the beam is technically challenging and reduces experimental data rates. Rastering the beam through a uniform pattern distributes the irradiation across the target, and the local irradiation time is inversely proportional to the transverse speed of the rastered beam.

High-energy (GeV) electrons lose energy within target material primarily through bremsstrahlung photons that leave the target without subsequent interaction. However, electron energy deposition within the target is predominatly through elastic (Møller) scattering from molecular electrons (see Figure 2). At electron beam energies of a few GeV, the energy deposition within a target comprised of solid HD with aluminum cooling wires (approximately 9:1 mass ratio) is approximately 2.2 MeV cm^2/g, or 2.2 mW for a 1 nA beam through 5 cm of target material.

As discussed in Appendix A, the resulting local temperature of the HD target material is approximately given by

$$T = \left(\frac{\alpha}{\upsilon} + T_{\mathrm{o}}^4\right)^{1/4} \tag{1.1}$$

where α is determined by characteristics of the target and beam (e.g. beam intensity, target cell geometry), υ is the transverse speed of the rastered beam across the target, and T_{o} is the equilibrium temperature at which the cooing power of the in-beam cryostat refrigerator is equal to the average heat load on the target. With the beam off, T_{o} is determined by residual heat conduction down the target's mechanical support and by radiative heating from surrounding heat shields. With the beam on, T_{o} is primarily due to the energy deposited in the target. For the in-beam cryostat, the beam-off T_{o} was about 50 mK; with a 1 nA electron beam on a g14 target, T_{o} was about

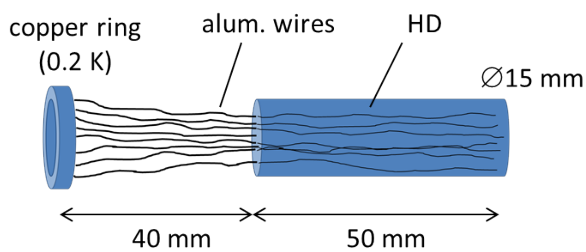

Figure 3: A schematic of the g14 target cells used during the 2012 eHD test runs. A cylindrical shell of polychlorotrifluoroethyene (not shown) surrounding the solid HD is glued into a copper cooling ring that is thermally coupled to the IBC mixing chamber. The HD is embedded with approximately 960 evenly spaced, 38 μm diameter aluminum wires of 5N purity that are soldered into the copper cooling ring, which provide a path for heat transfer from the HD to the IBC mixing chamber.

200 mK. Because the first term in Equation 1.1 usually dominates, a faster raster speed results in smaller temperature increases above T_{o}.

In order to minimize the temperature increase that results from electron beam interactions with the target, the local time-averaged energy deposition in the target should be divided into a series of brief irradiation pulses that each produce a small temperature increase in the target. The ideal case is one in which an energy deposition pulse begins prior to target cooling back to base temperature following the previous pulse, so that local maximum and minimum target temperatures deviate little from the average target temperature. Optimal target temperatures therefore depend on rastering speed and the cooling characteristics of the target.

As shown schematically in Figure 3, the g14 targets contained approximately 960 aluminum wires of 5N purity, 90 mm long and 39 μm in diameter. The wires were approximately evenly-spaced throughout the 50 mm long cylinder of HD and extend 40 mm to a copper cooling ring that couples to the IBC mixing chamber. Heat in the HD conducts along the aluminium wires and into the cooling ring and IBC mixing chamber. The 1 nA equilibrium temperature of approximately 200 mK is set by the heat load on the IBC mixing chamber from the g14 target. Aluminum was chosen because it is a low-Z material that has good thermal conduction at low temperatures, and its thermal conductivity increases with material purity.

The rate at which heat can be transferred from the HD to the mixing chamber depends on the length, diameter, purity, and number of aluminum wires in the target, and the density of wires within the HD. From a peak target temperature of 1 K, it takes about 0.1 s for the g14 target temperature to return to 200 mK; for 1.5 K, it takes around 0.4 s (see Figure 5). The length of time needed for the target to return back to base temperature is characteristic of the heat conduction along the aluminum wires. Lower peak temperatures can be produced by more frequent and briefer pulses generated by a fast raster, but to benefit from these improvements the heat conduction out of the target needs to be sufficient to allow for quick target cooling times.

1.1 Frequency-modulation rastering scheme

In general, the density of beam particles within a spot on target is inversely proportional to the transverse speed of the beam spot along its trajectory. For a cylindrical target, a spiral pattern provides optimal coverage, and uniform particle density along the spiral trajectory is obtained by requiring a constant transverse speed $v = \mathrm{d}s/\mathrm{d}t$, where $\mathrm{d}s$ is the spiral track element given by

$$\mathrm{d}s^2 = \mathrm{d}r^2 + r^2 \mathrm{d}\theta^2 \tag{1.2}$$

with angle θ and radius r.

One way to satisfy this condition is to require a constant radial pitch $\mathrm{d}r/\mathrm{d}\theta$. Assuming that the radial component of the transverse speed is much smaller than the azimuthal component (i.e. $v_r/v\theta \ll 1$), the condition of constant radial pitch can be satisfied with an angular rastering frequency ω given by

$$\omega(t) = \frac{v}{r(t)} \tag{1.3}$$

and radius

$$r(t) = \left(\frac{R_{\max}\, v\, t}{\pi\, N} \right)^{1/2} \tag{1.4}$$

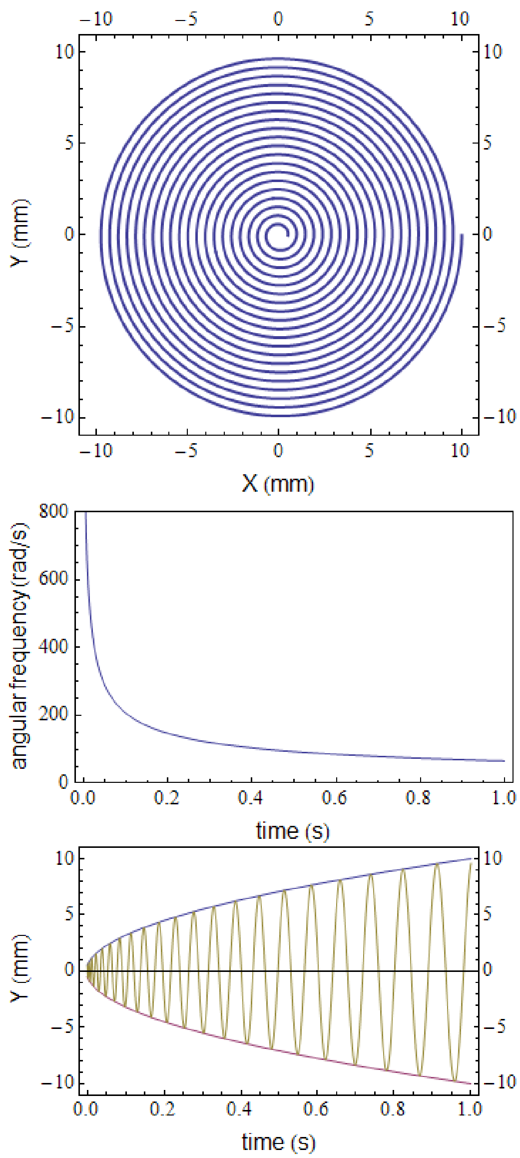

Figure 4: Plots of an FM-mode raster pattern with $R_{\min} = 0.5\,\mathrm{mm}$, $R_{\max} = 10\,\mathrm{mm}$, $N = 20$, and $v = 0.6\,\mathrm{m/s}$. The refresh rate for this pattern is 0.5 Hz (i.e. the time for tracing the pattern from $R_{\min}$ to $R_{\max}$ is 1 s, so the time to trace the full pattern and return to the initial position is 2 s). The top plot shows the beam spot trajectory on target. The middle plot shows the time variation of the angular frequency; the maximum frequency at $t = 0$ is around 1400 rad/s or 220 Hz. The bottom plot shows the time variation of the beam spot trajectory along the y-axis.

where $R_{\max}$ is the maximum radius of the pattern and N is the number of revolutions in the raster pattern. A more thorough derivation can be found in Reference [3].

In this rastering scheme, the angular frequency $\omega(t)$ is not constant and in fact grows infinitely large as the radius r goes to zero, so a non-zero minimum pattern radius $R_{\min}$ is needed. During operation, the rastered beam spot traces out a spiral pattern between $R_{\min}$ and $R_{\max}$ and back again with a specified cyclic time. Figure 4 shows a raster pattern on target, and the time variation of the angular frequency and displacement along the y-axis. Because the angular frequency $\omega(t)$ is periodically varied during rastering, this scheme is referred to as *frequency-modulation* or FM-mode.

The raster used during the 2012 eHD test runs (Hall B Slow Raster) used a FM-mode spiral rastering scheme with a 99-turn pattern that started 1/2 turn from the center and a pattern refresh rate of 1 Hz. The angular frequency varied between 19.8 kHz at $R_{\min}$ and 100 Hz at $R_{\max}$.

At a distance of approximately 23 m from CLAS center, the Hall B Slow Raster produced a 5 mm radius pattern on the g14 target with a transverse speed of 3.1 m/s. For a 1 nA beam, the calculated local peak temperature of the target resulting from electron beam energy deposition was 1.43 K (see Figure 5). The IBC dilution fridge provided cooling, and the local target temperature dropped back to a base of 200 mK within about a half of a second after an irradiation pulse. This peak temperature is for the best case when irradiations are evenly spaced in time (i.e. locations midway between $R_{\min}$ and R_{mzx}). The peak temperature for the worst case was 1.62 K at target locations near $R_{\min}$ or $R_{\max}$, where the irradiations bunch up in time (in general, worst case peak temperatures are higher by 10-15%).

For a uniform raster pattern, there is a theoretical average target temperature that arises by setting the beam spot size equal to the pattern radius and assuming a uniform beam density profile. This is equivalent to an infinitely-fast raster with complete and uniform pattern coverage. This average temperature depends on the beam current and the geometry and thermal properties of the target, and is indepen-

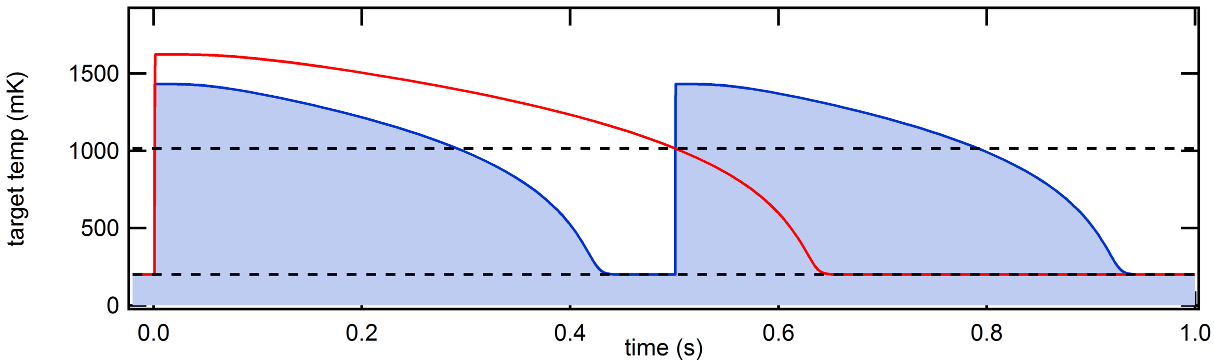

Figure 5: Plot of the calculated temperatures in the g14 target cell due to local heating from a 1 nA electron beam rastered by the Hall B Slow Raster with a 5 mm radius pattern. The red curve corresponds to local target temperatures at locations either near the center or the periphery of the raster pattern, while the blue curve corresponds to target locations midway between the center and the periphery of the pattern. The dashed lines are the theoretical average target temperature (upper line) of 1.02 K and the base temperature of 200 mK maintained by the IBC (lower line).

dent of rastering speed. For the Hall B Slow Raster, the average temperature of the g14 target for a 1 nA beam and a pattern radius of 5 mm was 1.02 K. Increasing the pattern radius to 7.5 mm (the full extent of the g14 target) lowers the average temperature to 710 mK and peak temperatures to between 1.23 K and 1.40 K (best case and worst case peak temperatures, respectively).

Rastering speed does not affect the average target temperatures, but it does affect peak temperatures. Faster speeds produce briefer but more frequent irradiations with peak temperatures that deviate less from average target temperatures – faster rasters produce more uniform target temperatures.

As an example, consider the next-generation eHD target (see Figure 6) that has a 25 mm long cylinder of solid HD with a diameter of 25 mm, which is embedded with approximately 2000, 51 μm diameter aluminum wires of 5N-purity that are half the length of those in the g14 target. Using the Hall B Slow Raster with a 1 nA beam and a 12.5 mm radius raster pattern with refresh rate of 1 Hz, the IBC mixing chamber would provide a base temperature of 145 mK, and the average target temperature would be 233 mK with peak temperatures of 1.02 K to 1.16 K. Increasing the rastering speed to 100 Hz refresh rate would reduce the peak temperatures to 376 mK to 443 mK while leaving the average temperature the same (see Figure 7).

The Hall B Slow Raster uses a magnet coil wound with heavy-gauge, solid copper wire. Alternating currents (AC) generate EMFs within conductors that result in eddy-currents and associated power losses, and the magnitude of the eddy-currents increases with frequency and wire diameter[1]. At a 1 Hz refresh rate, the magnet coil momentarily experiences 19.8 kHz AC when the beam spot is near the center of the raster pattern but less than 500 Hz AC for the majority of the rest of the pattern. At these nominal and peak frequencies, the magnet wire can withstand the eddy-current heating.

However, increasing the speed of an FM-mode raster has limitations. At a refresh rate of 100 Hz, the Hall B Slow Raster would have to sustain 50 kHz AC and brief peaks of 2 MHz AC, which is unobtainable with its existing magnet coils due to eddy-current heating. The Hall B Slow Raster does not permit substantial improvements in rastering performance using FM-mode rastering. In order to access these faster speeds, a different raster or an alternate rastering scheme is needed.

The problems associated with heavy-gauge, solid

[1] Copper has a skin depth of $\delta = 65.5\ \text{mm}/(f_o)^{1/2}$

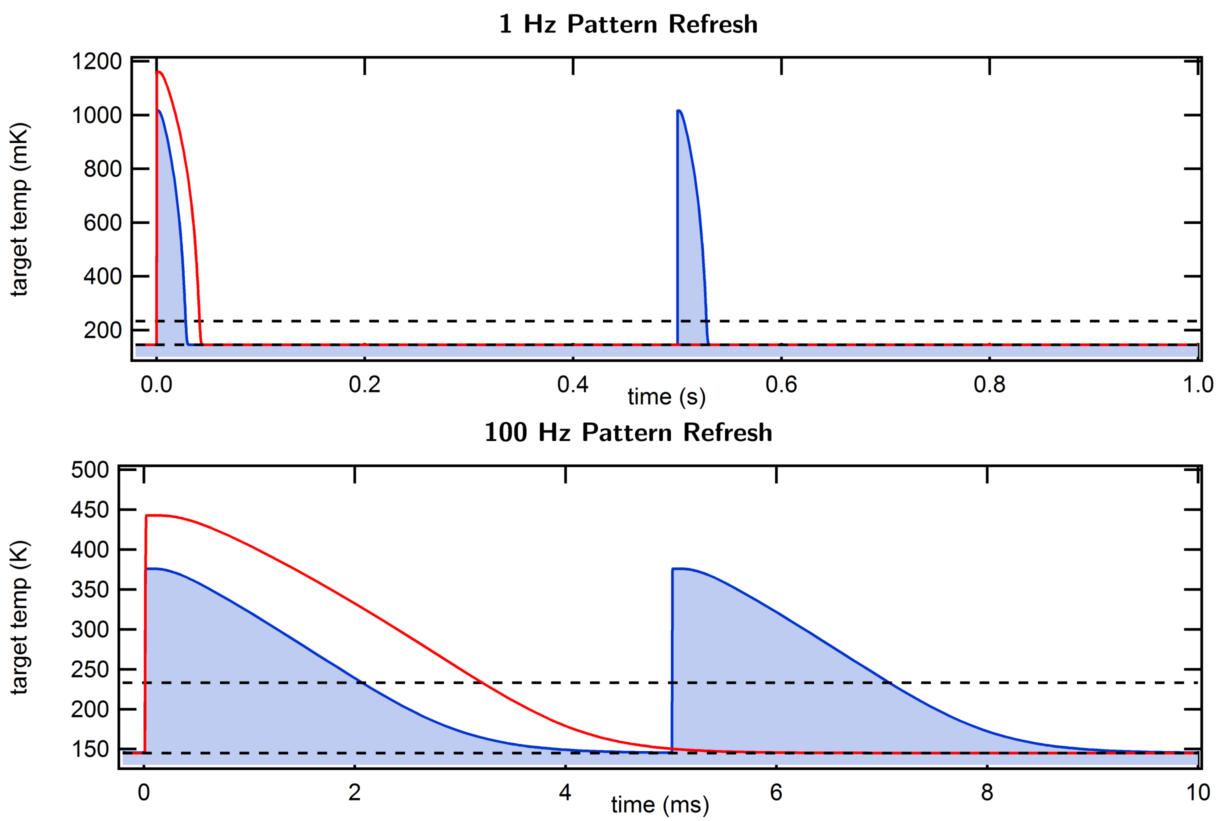

Figure 7: Plot of the calculated local target temperatures in a next generation HD target cell (as shown in Figure 6) due to a 1 nA electron beam rastered by an FM-mode raster with a 12.5 mm radius pattern. The top plot shows the result for a 1 Hz pattern refresh rate, and the bottom plot is for a 100 Hz refresh rate (NB. the plots have different time scales). The red curves corresponds to local target temperatures at locations near the center or the periphery of the raster pattern, while the blue curves correspond to locations midway between the center and the periphery of the raster pattern. The dashed lines indicate the theoretical average target temperature (upper line) of 233 mK and the base temperature of 145 mK maintained by the IBC (lower line).

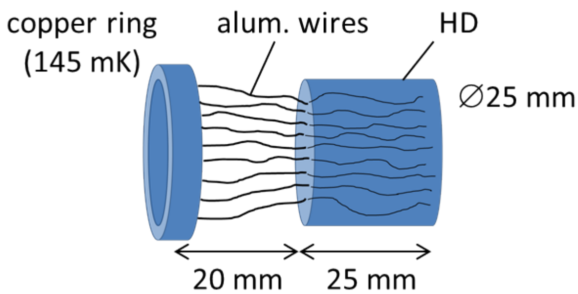

Figure 6: A schematic of a next-generation target cell for eHD experiments. The cylinder of solid HD is 25 mm long and 25 mm in diameter, and is embedded with approximately 2000 evenly spaced 51 μm diameter aluminum wires of 5N purity that are soldered into a copper cooling ring. The length of the aluminum wires between the HD and the cooling ring is 20 mm, which allows for improved heat transport compared to the g14 target design. A cylindrical shell of PCTFE (not shown) surrounds the solid HD and is glued into the cooling ring.

copper wire can be overcome by using *Litz*[2] cable, which consists of multiple wire strands that are individually insulated and is designed to reduce power losses due to eddy-currents. Litz cable employing 38 AWG strand copper wire can operate at AC frequencies up to 100 kHz, which would restrict the operation of a litz cable magnet coil in FM-mode to refresh rates below 10 Hz. Faster speeds may be possible, but eddy-current heating at the peak frequencies in the MHz range might result in catastrophic failure of the magnet.

1.2 Amplitude-modulation rastering scheme

An alternate method for satisfying the constant transverse speed requirement for uniform particle density in Equation 1.2 assumes a constant angular frequency $\mathrm{d}\theta/\mathrm{d}t$. The radius for this spiral pattern is given by

$$r(t) = R_{\max}\left(\frac{\omega\, t}{2\pi N}\right)^{1/2} \tag{1.5}$$

[2]The term "Litz" wire comes from Litzendraht, which is German for braided, stranded, or woven wire.

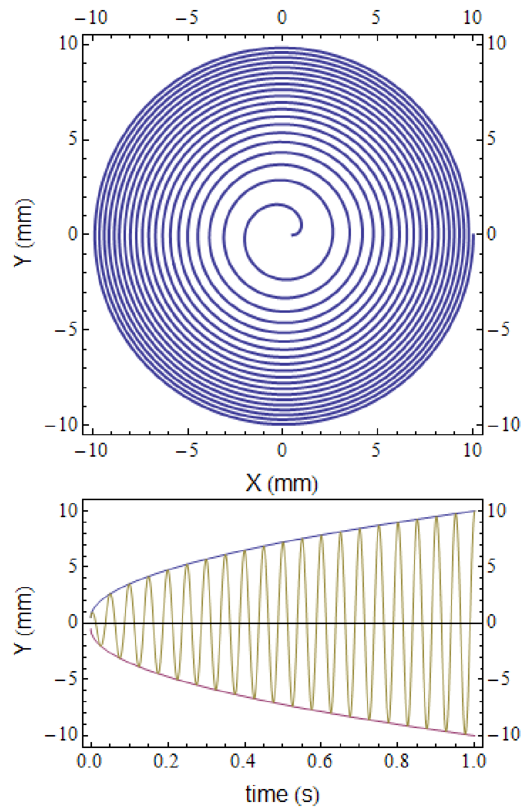

Figure 8: Plots of an AM-mode raster pattern with with $R_{\min} = 0.5\,\mathrm{mm}$, $R_{\max} = 10\,\mathrm{mm}$, $N = 20$, and $\upsilon = 0.5\,\mathrm{m/s}$ (eqn. 1.5). The refresh rate for this pattern is 0.5 Hz (i.e. the time for tracing the pattern from $R_{\min}$ to $R_{\max}$ is 1 s, and the time to trace the full pattern is 2 s). The top plot shows the beam spot trajectory on target. The bottom plot shows the time variation of the trajectory along the y-axis. The angular frequency is 126 rad/s or 20 Hz.

where $R_{\max}$ is the maximum radius of the pattern, $\omega = \mathrm{d}\theta/\mathrm{d}t$ is the angular frequency, and N is the number of revolutions in the raster pattern. A more detailed derivation can be found in Reference [4].

In this rastering scheme, the raster pattern radius follows a $\sqrt{t}$ dependence between a $R_{\min}$ and $R_{\max}$ like the FM-mode scheme; however, the radial pitch $\mathrm{d}r/\mathrm{d}\theta$ is no longer constant. Figure 8 shows a raster pattern on target and the time variation of the displacement along the y-axis. Because the beam deflection amplitude of a raster magnet (i.e. the radius $r(t)$ of the pattern) is periodically varied in time, this scheme is referred to as *amplitude-modulation*, or AM-mode.

The advantage of AM-mode rastering is the absence of high-frequency spikes. However, the disadvantage is the non-uniform coverage near the center of the raster pattern. This non-uniformity can be corrected by operating an AM-mode raster at higher frequencies or configuring the pattern to precess. In the case of the Hall B Slow Raster, the magnet coils cannot withstand the approximately 3 kHz AC required for reasonable pattern uniformity associated with a pattern refresh rate of 100 Hz. However, a magnet coil made from litz cable could be used to raster in AM-mode at pattern refresh rates up to 1 kHz. While improving the speed of the Hall B Slow Raster is not possible due to limitations of its magnet coil, substantial increases in speed are feasible with an AM-mode raster employing magnet coils made from litz cable.

2 Fast raster specifications

Loss of H- and D-polarization during eHD running is coupled the depolarization of unpaired electrons in HD^+ ions, which in turn is related to target temperature. During electron beam irradiation, the average target temperature is a function of beam current, raster pattern size, and target geometry. A redesigned target geometry and larger raster pattern would allow average target temperatures for a 1 nA beam to drop to 208 mK. However, rastering speed affects peak target temperatures as well as the uniformity of temperature in time, and faster rastering generates peak temperatures with smaller deviations away from the average target temperature.

In order to obtain substantial reductions in peak temperatures with the new HD target design, a raster needs to increase the pattern refresh rate by about a factor of 1000 over the current Hall B Slow Raster. An AM-mode raster with a a 900 Hz refresh rate and 24 kHz frequency could provide a uniform 12.4 mm radius pattern with a transverse speed of 1885 m/s (suitable for a 100 μm radius beam spot on a 12.5 mm radius target). The ratio of 900 Hz refresh rate to 24 kHz angular frequency allows the pattern to precess, which reduces the degree of non-uniformity near the center of the pattern. This raster configuration would produce peak target temperatures of 286 mK to 331 mK while maintaining an average target temperature of 233 mK (see Figure 9).

2.1 Low energy test runs

A design that incorporates a litz cable magnet coil and operates in AM-mode can achieve the desired performance. An existing 6-GeV fast raster [5, 6] previously used in Hall A and C has been operated at 24 kHz. Operational parameters for the 6-GeV Fast Raster are given in Table 1.

The 6-GeV Fast Raster system consists of two pairs of air-cooled *bedstead* coils, one each for the horizontal and vertical axes. The coils are mounted on a ceramic vacuum pipe, which avoids the eddy-current heating associated with the induced currents from high frequency magnetic fields. A thin coating of metal on the inner surface of the ceramic pipe conducts away the image current produced by the electron beam.

At 25 kHz, the 6-GeV Fast Raster is driven by a high voltage power supply controlled by an *H-bridge* power switch. This solid state switch produces a bipolar current waveform in the magnet coil that is approximately linear and is used to generate a square Lissajous raster pattern. Unfortunately, the H-bridge switch cannot produce a sinusoidal current waveform and so cannot generate a spiral raster pattern. However, the slow raster used in Hall A is driven at much lower frequencies by an LC resonant circuit that can generate an AM-mode spiral raster pattern. The supply consists of a power amplifier, a function genera-

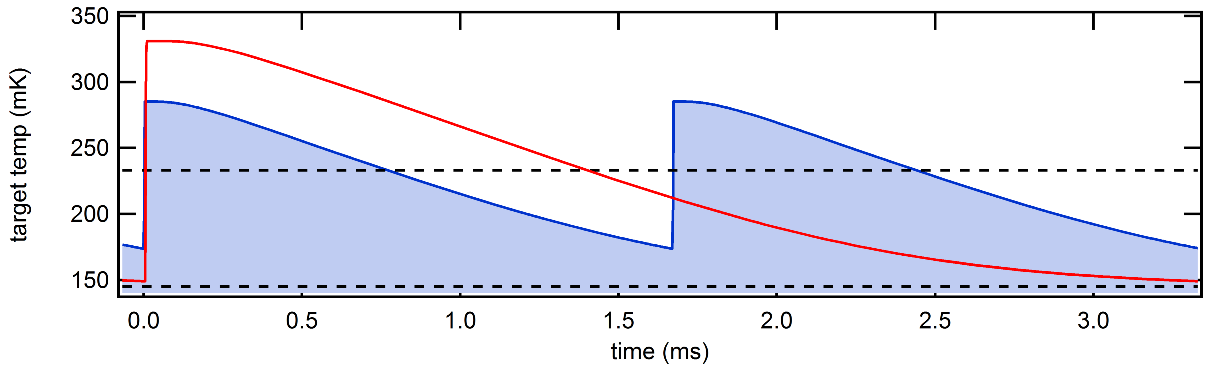

Figure 9: Plot of the calculated local target temperatures in the next generation HD target cell (as shown in Figure 6) due to a 1 nA electron beam spread over the target with an AM-mode raster with a 12.5 mm radius pattern and a 900 Hz refresh rate. The red curve corresponds to local target temperatures at locations near the center or the periphery of the raster pattern, while the blue curve correspond to locations midway between the center and the periphery of the raster pattern. The dashed lines indicate the theoretical average target temperature of 233 mK (upper line) and the base temperature of 145 mK maintained by the IBC (lower line).

tor, and a resonant-mode amplifier circuit made from an impedance converter (transformer) and a bank of resonant capacitors (see Figure 10). This resonance circuit could be modified to drive the 6-GeV Fast Raster magnet in AM-mode at a frequency of 24 kHz and a refresh rate of 900 Hz.

The 6-GeV Fast Raster uses two pairs of magnet coils to control the horizontal and vertical displacement of the beam, and each magnet coil pair is driven by its own LC resonant circuit. The power amplifiers for each circuit are controlled by a single function generator, and a circular pattern is generated by shifting the phase of the control signal for one of the power amplifiers by 90^{o} with a precision phase shifter. A current sensor on each magnet coil provides current measurement to the controller via a circuit protective device, and this signal can be used to trigger a fast shutdown sequence in the event of a raster failure.

The 6-GeV Fast Raster can produce a maximum of 0.353 mrad GeV of bending, and the calculated field map for one of the magnet coils is shown in Figure 11. For an eHD test run with a beam energy of at 1.1 GeV, this raster can generate a 7.4 mm radius pattern when positioned 23 m from CLAS center. For a 12.5 mm radius target, this pattern is too small. However, the use of a second identical 6-GeV Fast Raster located 22 m from CLAS center can increase the pattern radius to 14.4 mm, which is sufficiently large. Spare magnet coils and components at JLab could be used to assemble a second 6-GeV Fast Raster. Synchronization of both rasters can be accomplished using a common function generator for all magnet coils and the same precision phase shifter for signals going to the power amplifiers for coils of the same beam orientation (e.g. the vertical coils in both rasters).

3 11 GeV experiments

In the CLAS12 era, eHD experiments will use beam energies up to 11 GeV. At these energies, a dual 6-GeV Fast Raster can generate a pattern with a maximum radius of 1.4 mm. Nearly a factor of ten increase in raster performance is needed for complete target irradiation. Increasing the current in the 6-GeV Fast Raster coils would generate additional eddy-current heating. Because of the air-cooled configuration of the coils, any substantial increase in current could catastrophically damage the coils. At best, the 6-GeV Fast Raster coils could withstand only a modest increase in current, perhaps at the 5-10% level. A new raster system is needed at 11 GeV.

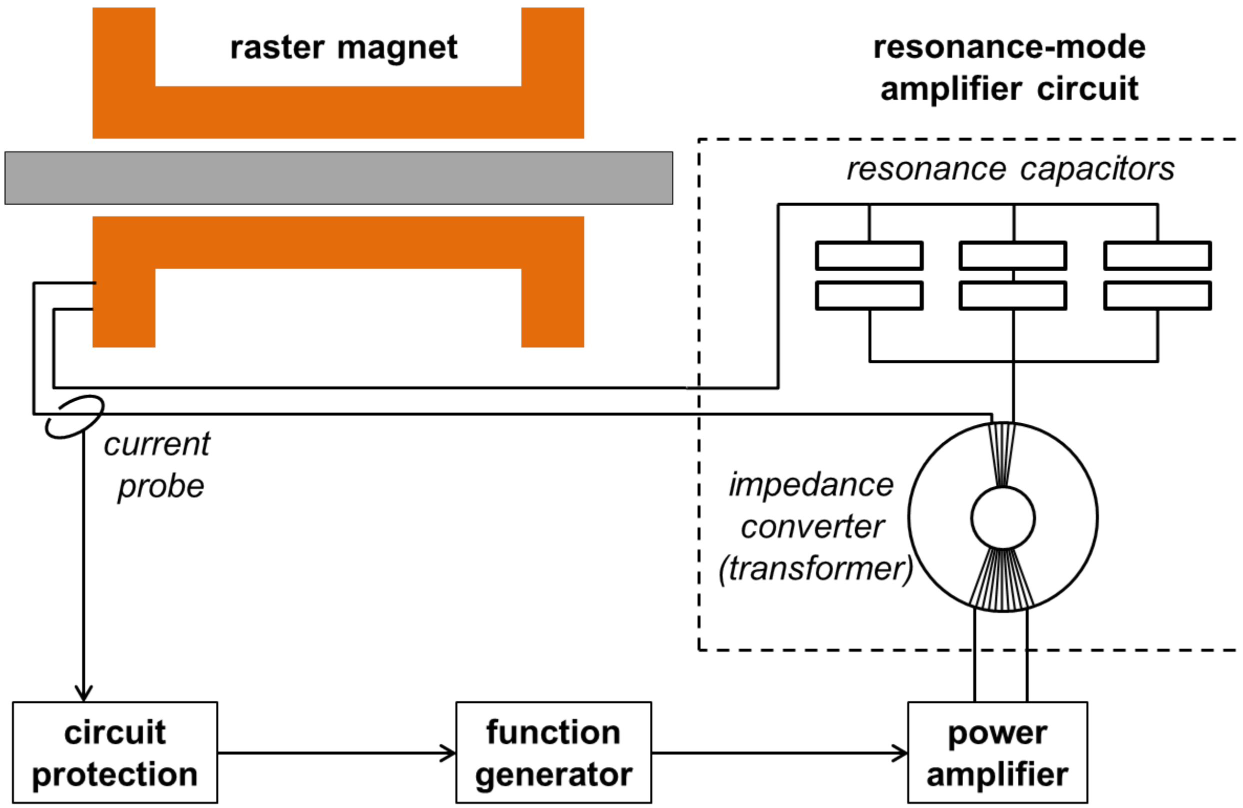

Figure 10: Block diagram of the resonance circuit used to drive an AM-mode circular raster. A power amplifier controlled by a function generator drives an LC resonant circuit that is tuned to the resonance frequency of the raster magnet coils and resonant capacitors, and their respective resistances. At the resonance frequency, the capacitive and inductance resistances are equal and tend to cancel each other so there is only the DC resistance of the circuit to oppose the applied current. A ferrite toroid transformer is used as an impedance converter to match the output impedance of the amplifier to the low input impedance of the resonant circuit. A sensor supplies current measurement to a circuit protection device.

Table 1: Specifications for AM-mode Fast Rasters

	6-GeV fast raster	11-GeV fast raster
$\int B \cdot dl$ (kG cm)	1.2	12.7
central field (G)	51.2	329
max bending angle (mrad GeV)	0.353	3.80
physical length (cm)	25	40
magnetic length (cm)	23.8	38.5
number of turns of litz 1650 conductor	12	38
inductance (mH)	0.088	1.4
DC resistance (Ω)	0.04	0.13
inductive reactance at 24 kHz (Ω)	13.3	13.4

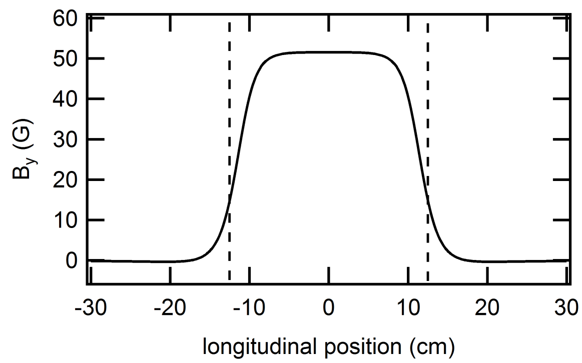

Figure 11: The calculated transverse field profile of the 6-GeV raster magnet along the beam axis. Modeling of the raster coil has been done in OPERA using data provided in references [5, 6], and field calculations have been done using TOSCA. The dashed lines indicate the physical extent of the 25 cm long magnet coils.

A new magnet coil could be based on the 6-GeV Fast Raster design and driven by an LC resonant circuit power supply similar to Figure 10. However, scaling up the design of the magnet coils to increase the bending power would increase the coil's impedance. The characteristics of the LC resonant circuit and power amplifier are coupled to the coil's impedance, and it is the performance of the power amplifier that constrains the maximum impedance of a magnet coil.

The bending power of a magnet coil is proportional to $\int B \cdot dl$, and its impedance is proportional to $N^2 Il$, where B is the magnetic field strength, l is the length of the coil, N is the number of turns, and I is the current in the coil. Assuming a new magnet coil would be constructed from the same type of litz cable as the 6-GeV Fast Raster, the current in the coil should remain about the same because of eddy-current heating effects. One approach to increasing the field strength would be to increase the number of turns on the coil by a factor of ten, but this would increase coil's impedance by a factor of 100, which is beyond the capabilities of the existing resonant circuits and power amplifiers.

Increasing the length of the magnet coil linearly increases the bending power and impedance. However, there are space limitations in the Hall B beam line. The dual 6-GeV Fast Raster configuration is about 2 m in length; a replacement 11-GeV fast raster should occupy roughly the same footprint in the beam line. Lengthening the magnet coils from 25 cm to 40 cm by mounting all of the coil pairs on a single ceramic beam pipe would increase the bending by 60% (n.b. each magnet coils of the existing 6-GeV Fast Raster is mounted on a separate beam pipe).

The use of a flux return around each coil could double the strength of the central field. Incorporating a flux return on the magnet coils requires the use a material with high permeability at rastering frequencies. Iron and steel are commonly used for magnet yokes because of their permeability and large maximum field (saturation); however, they cannot be used at high frequencies because of eddy-current heating.

Ferrites are a class of ceramic materials composed of metal and iron oxides that are easily magnetized and demagmetized and possess good permeability at high frequencies (see Figure 12). Ferrites are widely used in high-frequency (MHz) transformers. They have substantially lower saturation levels than iron or steel, so yoke design is critical for avoiding field saturation.

The addition of a ferrite yoke will increase the impedance of a magnet coil, however, for a thickness

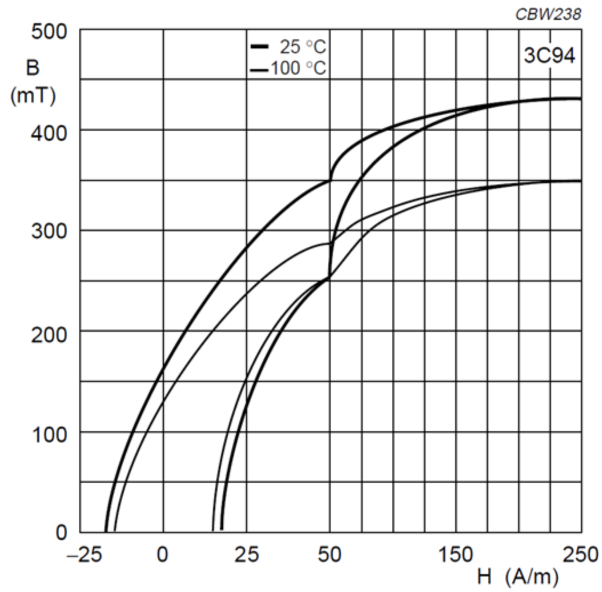

Figure 12: Plot of the B-H curve for type 3C94 MnZn ferrite as provided in the data handbook of Reference [7].

much smaller than the transverse dimensions of the magnet coils, the energy stored in the ferrite yoke is substantially less than the energy stored in the rest of the magnet, so the increase in inductance by adding a ferrite yoke in minimal.

Because the field saturation of ferrite is much smaller than that of iron or steel, care must be taken when designing a yoke. For type 3C94 MnZn ferrite, the saturation occurs around 4500 G. Potential critical points for saturation occur near interior corners or abrupt transitions between material thickness of the yoke and at the end of the yoke. Additional 10 mm thick ferrite slabs at each end of the magnet are designed to reduce the magnetic field strength at the ends of the yoke without significantly affecting the longitudinal fields along the electron beam path within the raster.

A new 11-GeV Fast Raster design based on a pair of 40 cm long, 38-turn coils with ferrite yokes could generate a 15.5 mm radius spiral raster pattern with an impedance 16 times that of the current 6-GeV Fast Raster; operational parameters are given in Table 1.

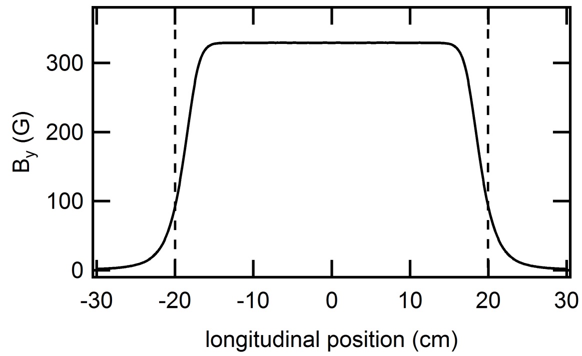

Figure 13: The calculated transverse field profile of the 11-GeV raster magnet along the beam axis. Modeling of the raster coil has been done in OPERA, and field calculations have been done using TOSCA. The dashed lines indicate the physical extent of the 40 cm long magnet coils.

The calculated field map for one of the magnets is shown in Figure 13. New magnet coils could be manufactured at JLab using the same methods that were previously used to build the 6-GeV raster, and the LC resonant circuit could also be built using the same design as the current 6-GeV raster.

The ferrite yoke would made from 10 cm thick, type 3C94 MnZn ferrite slabs on all four sides with additional 10 cm thick slabs on each end of the top and bottom walls for field shaping (see Figure 14). Type 3C94 MnZn ferrite is commercially available in dimensions compatible with this design. During operation of the 11-GeV raster, the magnetic field strength within this type of ferrite reaches a calculated maximum of 2200 G, which is well below the 4500 G saturation limit (see Figure 15).

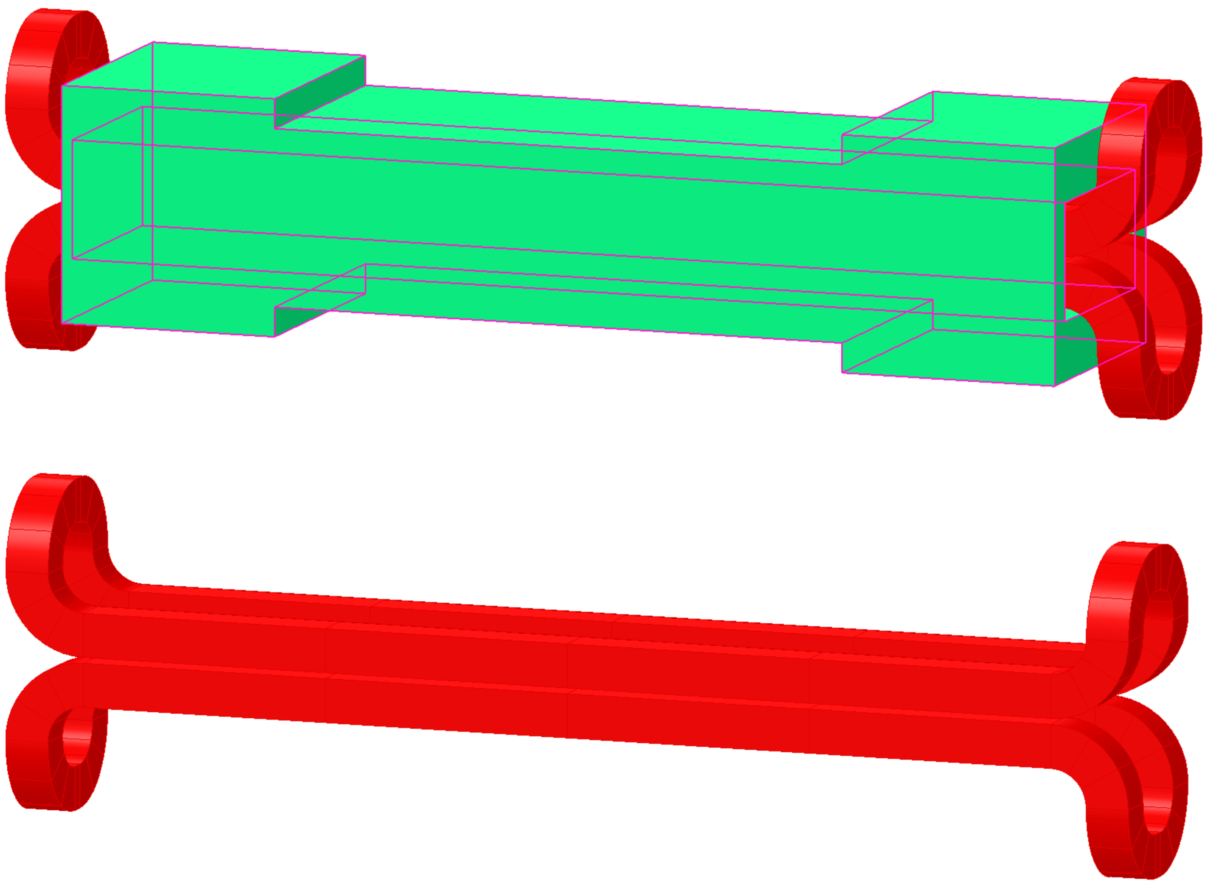

Figure 14: Drawings of the 11-GeV Fast Raster magnet. The top drawing shows the magnet coil (red) and the ferrite yoke (green), and the bottom drawing shows the geometry of the coil.

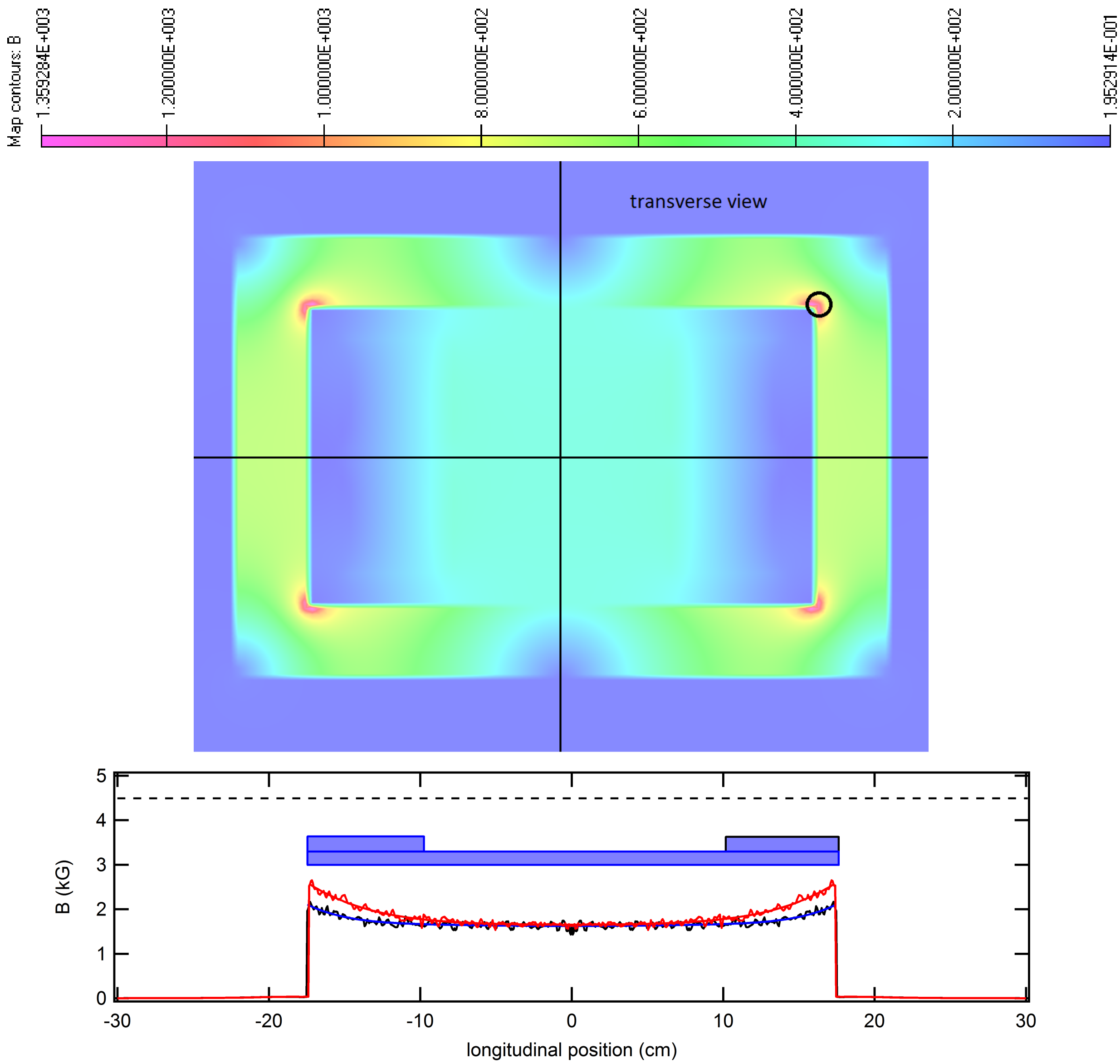

Figure 15: Plots of the total magnetic field strength within the ferrite yoke of the proposed 11-GeV raster magnet. Field calculations have been carried out with TOSCA. The top plot shows the field strength map for a transverse cross section at the center of the magnet. The largest field levels are within the interior corners of the yoke. The bottom graph shows the field strength at a position 0.5 mm within an interior corner of the yoke (indicated by a black circle on the top graph), plotted longitudinally along the magnet. The calculated field data is shown in black, and the smoothed data is shown in blue (the two are on top on each other in the above plot). A dashed line shows the 4500 G saturation level for the ferrite. Calculated and smoothed data in red show the total field strength along the yoke without the addition of the 10 mm thick ferrite plates at each end of the coil. Superimposed on the plot is a graphic of the cross-section geometry for the top of the yoke to illustrate field shaping effects (the vertical scale for the graphic is not to scale).

A Local temperature rise in HD due to electron beam heating

This estimation of localized target heating from electron beam energy deposition along its raster scan trajectory assumes that the heating is adiabatic and instantaneous. The target is a composite of solid HD and aluminum wires, and the electron beam energy deposition is different for each material, which results in different heating for the HD and aluminum. However, the time scale for energy deposition and heating is brief – a few microseconds – compared to the heat transport within and between materials, so the rise in temperatures for each material can be considered independent and instantaneous for calculation purposes.

The local temperature rise ΔT within target material due to the energy deposition of an electron beam along its trajectory can be calculated by

$$\Delta T = \frac{Q}{M \langle C_{\mathrm{p}} \rangle} \tag{A.1}$$

where Q is the electron beam deposited energy within a volume of target material during the beam dwell time Δt, M is the mass of the material within the volume, and $\langle C_{\mathrm{p}} \rangle$ is the material temperature-averaged heat capacity. The electron beam deposited energy is given by

$$Q = \Delta P \, \Delta t \tag{A.2}$$

where ΔP is the electron beam deposited power in the target material during the dwell time. The deposited power is determined by

$$\Delta P = \frac{\mathrm{d}E}{\mathrm{d}x} L \, \rho \, I \tag{A.3}$$

where $\frac{\mathrm{d}E}{\mathrm{d}x}$ is the electron energy deposition within a material, L is the target length, ρ is the material mass density volume, and I is the electron beam current. Combining equations A.1, A.2, and A.3 produces

$$\Delta T = \frac{\mathrm{d}E}{\mathrm{d}x} \, \frac{L \, \rho \, I \, \Delta t}{M \langle C_{\mathrm{p}} \rangle} \tag{A.4}$$

The mass of material within the irradiated volume is given by

$$M = \eta \, L \, \rho \, \frac{\pi}{4} \, d^2 \tag{A.5}$$

where η is the mass fraction of a particular material within the irradiated volume (e.g. for the g14 target, η_{HD} is $\sim$90%, and η_{Al} is $\sim$10%), and d is the electron beam diameter. The transverse beam speed υ at the target is equal to $d/\Delta t$. Combining equations A.4 and A.5 with the transverse beam speed yields an expression for the increase in material temperature:

$$\Delta T = \frac{4}{\pi} \frac{\mathrm{d}E}{\mathrm{d}x} \frac{I}{\eta \, d \, \upsilon} \frac{1}{\langle C_{\mathrm{p}} \rangle} \tag{A.6}$$

The heat capacities for both the HD [8] and aluminum [9] are temperature-dependent, and their temperature-averaged heat capacities $\langle C_{\mathrm{p}} \rangle$ depend on the initial target equilibrium temperature T_{o} and material temperatures T after beam heating.

$$\langle C_{\mathrm{p}} \rangle = \frac{\int_{T_o}^{T} C_{\mathrm{p}} \, \mathrm{d}T}{\int_{T_o}^{T} \mathrm{d}T} \tag{A.7}$$

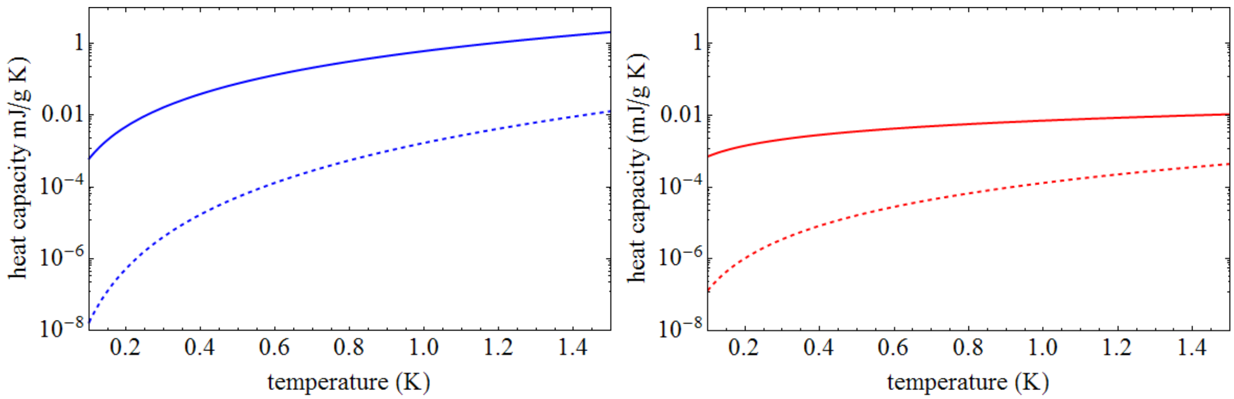

Figure 16: Plots of the calculated heat capacities for HD (left) and aluminum (right). The leading term for each heat capacity (T^3 for the HD, and T for aluminum) is displayed with a solid line and the next leading order term (T^5 for the HD, and T^3 for aluminum) is displayed with a dashed line.

The heat capacity for solid HD and aluminum for temperatures below 4 K are given below:

$$C_\mathrm{p}[\mathrm{HD}] = (1.87\,T^3 + 0.004\,T^5)\,\frac{\mathrm{mJ}}{\mathrm{mol\,K^n}} = (0.623\,T^3 + 0.0013\,T^5)\,\frac{\mathrm{mJ}}{\mathrm{g\,K^n}}$$
$$C_\mathrm{p}[\mathrm{Al}] = (1.35\,T + 0.02485\,T^3)\,\frac{\mathrm{mJ}}{\mathrm{mol\,K^n}} = (0.0500\,T + 0.0009213\,T^3)\,\frac{\mathrm{mJ}}{\mathrm{g\,K^n}}$$

As shown in Figure 16, the leading terms of the heat capacities for HD and aluminum dominate at temperatures below 1.5 K, so their temperature-averaged heat capacities $\langle C_\mathrm{p} \rangle$ can be approximated using their leading terms.

Combining equations A.6 and A.7 with the leading term approximation for heat capacity, the HD temperature following electron beam energy deposition can be expressed as

$$T_\mathrm{HD} \cong \left(\frac{\alpha_\mathrm{HD}}{\upsilon} + T_o^4\right)^{1/4} \tag{A.8}$$

$$\alpha_\mathrm{HD} = (8.175\,\mathrm{K}^4\,\mathrm{g/mJ})\,\frac{\mathrm{dE}}{\mathrm{dx}}\,\frac{\mathrm{I}}{\eta_\mathrm{HD}\,\mathrm{d}}$$

where υ is the transverse speed of the beam spot on the target, and α is determined by the beam parameters and target characteristics (i.e. heat capacity, mass fraction of HD in the target η_{HD}, and electron energy deposition within HD). Similarly, the aluminum temperature can be expressed as

$$T_\mathrm{Al} \cong \left(\frac{\alpha_\mathrm{Al}}{\upsilon} + T_o^2\right)^{1/2} \tag{A.9}$$

$$\alpha_\mathrm{Al} = (1.886\,\mathrm{K}^2\,\mathrm{g/mJ})\,\frac{\mathrm{dE}}{\mathrm{dx}}\,\frac{\mathrm{I}}{\eta_\mathrm{Al}\,\mathrm{d}}$$

The mass fraction of aluminum in the target η_{Al} is of order 10%. Because of the lower average density of aluminum in the target ($\sim \rho_{Al}/100$), the energy deposited in HD is about ten times the energy deposition in aluminum. Thus, the target temperature after electron beam energy deposition can then be approximated by equation A.8.

References

[1] GEANT 3.2.1, CERN Library W5013 (1993).

[2] Stopping-power and range tables for electrons program, available online at physics.nist.gov/PhysRefData/Star/Text/ESTAR.html

[3] M. Fukuda, S. Okumura, and K. Arakawa. Nucl. Instrum. Methods A **396** (1997) 45-49.

[4] Y.K. Batygin, V.V. Kushin, and S.V. Plotnikov. Nucl. Instrum. Methods A **363** (1995) 128-130.

[5] C. Yan *et al.* Proc. Part. Accel. Conf. **4** (1993) 3109-3105.

[6] C. Yan, N. Sinkine, and R. Wojcik. Nucl. Instrum. Methods A **539** (2005) 1-15.

[7] Soft Ferrites and Accessories 2009 Data Handbook. Ferroxcube, Yageo Corp. www.ferroxcube.com.

[8] J.H. Constable, A.Q. McGee and J.R. Gaines. Phys. Rev B **11** (1975) 3045-3051.

[9] N.Phillips, Phys. Rev. **114** (1959) 676.